Current Research in Microbial Sciences 3 (2022) 100103

Contents lists available at ScienceDirect

Current Research in Microbial Sciences

journal homepage: www.sciencedirect.com/journal/current-research-in-microbial-sciences

Preparation, urease inhibition mechanisms, and anti-*Helicobacter pylori* activities of hesperetin-7-rhamnoglucoside

Mohamed Sharaf [a,b], Muhammad Arif [a], Hamed I. Hamouda [c,d,e], Sohaib Khan [a], Mohnad Abdalla [f,*], Samah Shabana [a], Hussein. E. Rozan [a,b], Tehsin Ullah Khan [a], Zhe Chi [a], Chenguang Liu [a,*]

[a] Department of Biochemistry and Molecular Biology, College of Marine Life Sciences, Ocean University of China, Qingdao, 266003, PR China
[b] Department of Biochemistry, Faculty of Agriculture, Al-Azhar University, Nasr City, Cairo, 11751, Egypt
[c] College of Food Science and Engineering, Ocean University of China, Qingdao, 266003, China
[d] Processes Design and Development Department, Egyptian Petroleum Research Institute, Nasr City, 11727, Cairo, Egypt
[e] University of Chinese Academy of Sciences, Beijing, 100039, China
[f] Key Laboratory of Chemical Biology (Ministry of Education), Department of Pharmaceutics, School of Pharmaceutical Sciences, College of Medicine, Shandong University, 44 Cultural West Road, Shandong Province, 250012, PR China

ARTICLE INFO

Keywords:
Helicobacter pylori
Hesperidin
Antimicrobial
Anti-urease
Molecular docking
Molecular dynamics simulation

ABSTRACT

This work investigated the effects of the bioflavonoid hesperetin-7-rhamnoglucoside isolated from *Citrus uranium* fruit peel on *Helicobacter pylori* (*H. pylori*). Separation and purity, crystalline state, and urease inhibition assays were carried out. Then, molecular docking and molecular dynamics (MD) simulations were conducted with urease as the target protein. Hesp was isolated from citrus peel with a purity of 95.14 μg mg^{-1} of dry raw material. X-ray diffraction analysis, hydrogen-1 nuclear magnetic resonance, Fourier transform infrared spectroscopy, and differential scanning calorimetry revealed that pure Hesp had the same crystallinity rating as the Hesp standard. The kinetic inhibition study demonstrated that Hesp inhibited *H. pylori* urease in a competitive and concentration-dependent manner with jack bean urease. In addition, bioimaging studies with laser scanning confocal microscopy and scanning electron microscopy illustrated that Hesp interacted with bacterial cells and induced membrane disruption by creating holes in the outer membranes of the bacterial cells, resulting in the leakage of amino acids. Importantly, molecular docking and 20 ns MD simulations revealed that Hesp inhibited the target protein through slow-binding inhibition and hydrogen bond interactions with active site residues, namely, Gly11 (O···H distance = 2.2 Å), Gly13 (O···H distance = 2.4 Å), Ser12 (O···H distance = 3.3 Å), Lys14 (O···H distance = 3.3 Å), and Arg179 (O···H distance = 2.7 Å). This work presents novel anti- *H. pylori* agents from natural sources.

1. Introduction

Helicobacter pylori is one of the most dangerous Gram-negative bacteria that cause numerous digestive system disorders, including chronic gastritis and diseases with severe complications, such as gastric cancer (Matysiak-Budnik and Mégraud, 2006; Amieva and Peek Jr, 2016). *H. pylori* urease (*HpUre*) has the chemical structure of urea amidohydrolase (E.C. 3.5.1.5) and induces the hydrolysis of urea and the rearrangement of ammonia and carbonate; it naturally breaks down at a typical functioning pH and yields another ammonia molecule and bicarbonate (Mobley and Hausinger, 1989). Its activity contributes to the growth of colonies and the occurrence of peptic ulcers (Babu et al., 2017).

Chronic gastritis and peptic ulcers caused by *H. pylori* increase the rate of death due to gastric carcinoma to nearly 90% in the world's population (Hooi et al., 2017). *H. pylori* eradication is a good strategy for reducing gastric cancer risk in patients (Piazuelo et al., 2010; Parreira et al., 2016). Given that effective monotherapeutic substances for treating *H. pylori* infection are unavailable, current treatment for *H. pylori* relies on a combination of antibiotics, such as clarithromycin, amoxicillin, and metronidazole, and acid-suppressive drugs, such as proton-pump inhibitors (Savoldi et al., 2018). However, the eradication

* Corresponding author.
E-mail addresses: mohnadabdalla200@gmail.com (M. Abdalla), liucg@ouc.edu.cn (C. Liu).

https://doi.org/10.1016/j.crmicr.2021.100103

Available online 29 December 2021

rates of this therapeutic scheme have been declining to unacceptable levels (Malfertheiner et al., 2017) mostly because of high antibiotic resistance levels. *H. pylori* is one of the 16 antibiotic-resistant microbes that pose notable danger to human life (Dang and Graham, 2017).

Medication bioavailability, tolerance, biofilm and coccoid formation of strains with various antibiotic susceptibilities affect the effectiveness of anti-*H. pylori* therapy (Tshibangu-Kabamba and Yamaoka, 2021). Additionally, complex regimens require daily administration of multiple doses of medications, thus decreasing therapeutic compliance. Hence, novel treatment approaches are required (Debraekeleer and Remaut, 2018).

Bioactive antibacterial compounds derived from natural sources, such as plants or marine organisms, may be useful in developing highly effective strategies for treating *H. pylori* infection (Parreira et al., 2018). Natural compounds have played a pivotal role in traditional medicine for centuries, and developments in the medical field in the last decades have led to a renewed interest in these compounds. Advances in chemical characterization, comprehensive activity screening, and the creation of stomach-specific delivery strategies have aided their application to gastric infection control (Parreira et al., 2016).

Many published studies revealed the therapeutic potential of various plant extracts and plant-derived compounds, such as flavonoids, for ulcer, *H. pylori* infection, and gastric malignancies (Salehi et al., 2018; Abou Baker, 2020; de Mendonça et al., 2020).

Naturally occurring flavonoids exhibit urease inhibitory uneven effects against *H. pylori* (Kataria and Khatkar, 2019). Flavone glycosides in Chinese herbal medications have a long history of use as therapeutic agents for preventing and treating many diseases (Basu et al., 2020). The development of an excellent progressive urease inhibitor agent for preventing bacterial growth and compact biofilm formation has attracted interest. Flavonoids exhibit excellent inhibitory activity against urease by interacting with the enzyme and blocking its interaction with its corresponding natural and synthetic substrates (Krajewska and Brindell, 2016).

Fruit and peel extracts of citruses, such as *Citrus lemons* and *Citrus uranium*, grapefruit, and sweet orange, contain hesperidin (Hesp), a β-7-rutinoside of hesperetin and a major bioflavonoid compound with the chemical formula hesperitin 7-rhamnoglucoside (Figs. S1A and B; (Hajialyani et al., 2019). The Hesp structure contains OH groups at C-3 and C-6', OCH_3 at C-5', and a glycoside moiety at C-3 (Naif and Ismail, 2018). Hesperetin has inhibitory effects against five *H. pylori* reference strains (ATCC 49503, ATCC 43504, ATCC 700392, ATCC 51932, and SS1; (Kim et al., 2021). Similar to other natural flavonoids, Hesp produced through the fungal enzymatic transmutation of various citrus species inhibits the growth of *H. pylori* ATCC 43504, NCTC 11637, NCTCII 638, 82548, 4, and 82516 at a final concentration of 0.3 mg mL^{-1} in vitro, reduces urease activity by 11% and 57%, respectively, and inhibits human gastroenteric maltase and HMG-CoA reductase (Bae et al., 1999; Gardana et al., 2008; Lee et al., 2012; Filocamo et al., 2015).

Few studies that performed systematic inquiries into the use of Hesp as an *H. pylori* antiurease (Zhang et al., 2008; Biglar et al., 2014; González et al., 2019) focused on the building blocks of the compound and performed *in silico* research through molecular docking and molecular dynamics (MD) simulations. Therefore, the present study aims to separate and distinguish Hesp from *C. uranium* peel as a nature-derived bioactive substance with important antibacterial efficiency for the development of novel and promising strategies for eradicating *H. pylori* without disrupting normal flora.

2. Materials and methods

2.1. Chemicals and reagents

Hesp standard (96%), Hanks' balanced salt solutions (HBSS), and phosphate-buffered saline (PBS) were purchased from Solarbio Science and Technology, China. AMX was bought from Sigma Aldrich (St. Louis, Mo., U.S.A.). Nutrient broth medium was acquired from OXOID, U.K. Phosphotungstic acid was procured from Sciences, Fort Washington, PA. All experiments were carried out by using sterile deionized water (Milli-Q).

2.2. Microorganism culture conditions

The isolated human *H. pylori* strain ATCC 700392 was provided by the Department of Medical Biochemistry and Biophysics (Umeã Uni, SWE). *H. pylori* was cultured at 37°C for 48–72 h on plates containing blood medium under a microaerophilic atmosphere. Colonies were collected and assembled in HBSS (pH 6.0) at an optical density of 0.06–600 nm (OD_{600}), which was ~10^7 (CFU) mL^{-1}, and then utilized in the following experiments. The optical density of the cultures was determined by using UV–Vis spectroscopy (TU 1810, Beijing, China).

2.3. C. uranium material collection

C. uranium fruit was purchased from a local market in Qingdao, China, peeled, and dried in an oven at 40°C–60°C for 30 min.

2.4. Extraction and separation of Hesp

First, 250 g of powdered citrus peel was placed in a Soxhlet unit reflux condense sleeve after the placement of glass wool. Then, 800 mL of petroleum ether (40°C–60°C) in a round flask was used for the first step of extraction, which was conducted for 4 h. The petroleum ether extract was discarded, and the adherent petroleum ether was removed by placing the content of the extraction sleeve in an extensive crystallization dish for 30 min. The filtrate was placed again in the Soxhlet unit with 800 mL of methanol for 1–2 h until its extract became colorless. After the extraction was completed, the extract was concentrated for 1 h with a rotary evaporation to separate the crude product and then acidified with 6% glacial acetic acid (pH 3–4). The concentrated residual liquid was kept in a refrigerator (4°C–6°C) overnight until a solid crystalline substance appeared. Finally, the residue was filtered, and a Buchner funnel was used to separate pure Hesp in the form of a powder. Physical and analytical tests were performed for characterization and identification (Chaudhry et al., 2016) (Scheme 1).

2.5. Evaluation of Hesp purity

Hesp purity was evaluated through HPLC analysis in accordance with a previous work (Husak et al., 2017; Marchyshyn et al., 2017). HPLC was carried out with a GBC 1100 Series HPLC equipped with a UV detector. Hesp was separated using a C18 column (250 mm × 4.6 mm; 5 μm). The mobile phase consisted of 10.2% acetic acid in 2 mM sodium acetate (solvent A) and acetonitrile (solvent B). The injection volume was 50 μL, and the flow rate was 1 mL min^{-1} at 25°C. The wavelength for flavonoid observation was 275 nm.

2.6. Characterization of crystalline Hesp status

The pure Hesp and Hesp extract were mounted on a sample holder, and diffractograms were collected using an X-ray diffraction (XRD) system (D/max-rB, Rigaku, Japan) from 2θ of 3° as the initial angle to 2θ of 50° as the final angle at a scanning speed of 4° min^{-1}.

A single-pulse sequence was used in obtaining hydrogen-1 nuclear magnetic resonance (^{1}H-NMR) spectra under the following conditions: acquisition time of 2.18 s, X offset of 4.7 ppm, achievement point of 16 384, scan number of 16, and relaxation delay of 15 s. The 90° pulse width of the bioflavonoid Hesp was determined linearly by using a single-pulse sequence under the above conditions at a pulse width setting of 41.0–44.0 μs at 0.1 μs intervals. The spin-lattice relaxation delay value of 1 mM Hesp was measured in 10% DMSO-d6 in an array experiment by using an inversion-recovery pulse sequence (Caligiani

et al., 2007) with a 30 s relaxation delay.

All spectra were referenced to the signal of DSS-d6 at 0.0 ppm. The spectrum of influential functional groups in the Hesp standard and Hesp extract was recorded through Fourier transform infrared spectroscopy (FT-IR, Shimadzu IRAffinity, Japan). Crystal KBr material was used for the preparation of samples with the disc method.

Differential scanning calorimetry (DSC) was performed with a DSC Q2000 instrument (TA Instruments, USA). An empty aluminum pan was utilized as a guide. Approximately 2–3 mg of samples was heated at 10°C min^{-1} (25°C–300°C) under nitrogen atmosphere (flow rate of 50 mL min^{-1}; (Sheng et al., 2019).

2.7. Urease inhibition assay

The concentration of ammonia was determined using the Berthelot method with phenol–hypochlorite reaction (Tanaka et al., 2003), which produces a colorimetric product that is measureable at 630 nm and whose amount is proportionate to urease activity in the presence of the inhibitor Hesp. Herein, the reaction buffer (10 μL of 50 mM K_2HPO_4 buffer [pH = 7.0] and 10 μL of ddH_2O) were added to each well of a 96-well plate. Jack bean urease (JBU, 1 μg μL^{-1}) was freshly prepared with 50 mM phosphate buffer. Then, 20 μL of the enzyme and 10 μL of the tested inhibitor (2.5–20 μg μL^{-1}) were poured in the reaction mixture. The mixture was incubated at 37°C for 10 min. Enzymatic reactions were started after the addition of 40 μL of the urea substrate and incubation at 37°C for 10 min. Urea concentrations (0.156–20 mM) were determined on the basis of urease activity under optimal conditions. Thiourea was used as a positive control reference at concentrations of 1.56–100 mM. Then, 80 μL of reagent 1 (0.5% sodium hydroxide in 0.1% sodium hypochlorite [active chlorine]) and 50 μL of l reagent 2 (0.005% w/v sodium nitroprusside, 1.0% w/v phenol) were added to the tested wells and kept at room temperature (approximately 20°C–22°C) for 50 min. The amount of liberated ammonia from the reaction mixtures was detected at 625 nm with a microplate reader (BioRad, Washington, USA) and then calculated on the basis of the calibration curves. Inhibition (%) was calculated in accordance with the following equation:

$$Inhibition\ \% = \left[1 - \frac{AT}{Ac}\right] \times 100, \quad (1)$$

where A_T is the absorbance value of the well containing the inhibitory compound and A_C is the absorbance of the reaction mixture without the inhibitory compound. The IC_{50} values of Hesp were calculated using nonlinear regression (curve fit) and dose–response inhibition in Graphpad Prism 8.0.2 software (San Diego, CA, USA).

2.8. Determination of the kinetic parameters of urease activity

The binding mechanism of the inhibitor (Hesp) to urease was determined on the basis of the Lineweaver–Burke plot for the evaluation of kinetic properties. The activities of the enzymes were measured against the gradient concentrations of Hesp (2.5–100 μg μL^{-1}) in 50 mM PBS (PBS pH 7) at 37°C for 10 min. A total of 10 μL of Hesp was incubated with 40 μL of the substrate at an appropriate concentration (2.5–100 μg μL^{-1}), and whether Hesp had a noncompetitive, uncompetitive, or competitive binding mechanism was determined (Imran et al., 2020). Activity was determined for the calculation of initial velocities. Graphpad Prism was used in plotting the initial rate against substrate concentrations. The apparent kinetic constants (K_m) and maximum reaction velocity (V_{max}) values were calculated by plotting 1/v versus 1/urea with nonlinear regression methods. Inhibitory constants (K_i) for Hesp plots were determined as the intersection on or corresponding to the X-axis of the plots of 1/V versus the inhibitory constants (Ki) that was calculated in accordance with the following equation:

$$Slope\ [\mathrm{m}] = \frac{[Km]}{[S] + [Km]} + \frac{1}{[Ki]}. \quad (2)$$

All experiments were conducted in triplicate.

2.9. In situ visualization of antimicrobial properties

2.9.1. Laser scanning confocal microscopy

H. pylori ATCC 700392 cells were detected by using LIVE/DEAD BacLight bacterial viability kits with slight modifications (Arif et al., 2021b). *H. pylori* ATCC 700392 was treated with 150, 250, and 500 μg mL^{-1} Hesp for 24 h. Subsequently, equal quantities of SYTO 9 (for living cells) and propidium iodide (for dead cells) solution were added. Then, the sample was maintained in the dark for 30 min. The sample was observed through laser scanning confocal microscopy (LSCM, Leica TCS SP5 II, Leica, Wetzlar, Germany) with an excitation wavelength between 488 and 560 nm. Chambers were visualized with Zeiss LSM 410 with a 63 × 1.4 NA oil objective lens. Zengreen and Zenred imaging was used in capturing and analyzing images of *H. pylori*. ImageJ analysis software (National Institute of Health, USA) was used in processing. The control was *H. pylori* ATCC 700392 in sterile PBS (pH 7.4) without Hesp. The binding and conjugation of the fluorescent dye FITC with the damaged cell membranes of Hesp-treated *H. pylori* were investigated in accordance with a previous method (Cai et al., 2015) with slight modifications. At 4°C, the Hesp-treated *H. pylori* ATCC 700392 strain was centrifuged for 6 min at 8000 rpm. Subsequently, the supernatant was incubated with FITC-I (a green fluorescent dye) for 30 min at 37°C in the dark. Then, for CLSM photography, 25 μL of the sample was mounted on a glass slide (Leica TCS SP5 II, Leica, Wetzlar, Germany).

2.9.2. Scanning electron microscopy analysis

First, the control (untreated bacterial cultures) and the cells treated with 150, 250, and 500 μg mL^{-1} Hesp solution were incubated at 35°C ± 2°C for 12 and 24 h. The cells were harvested in triplicate through centrifugation at 3500 rpm for 3 min and washed with 100 mM (PBS pH 7.4). Then, the bacterial cell pellet was blended overnight at 4°C ± 0.5°C with 500 μL of 2.5 % (v/v) glutaraldehyde for 2 h. The bacterial samples were postfixed in 1.0% osmium tetroxide for 1 h at 4.0°C before they were washed with PBS (pH 7.4).

Subsequently, the specimens were dehydrated for 10 min with varying amounts of ethyl alcohol (40%, 60%, 80%, and 100%) and then washed with PBS (pH 7.4). The samples were dehydrated to the critical stage after being washed twice with 1:1 (v/v) ethanol:butanol solution and spread in 100% pure butanol. Finally, the bacterial samples were covered with a 200 Å Au film, and a micrograph was obtained through scanning electron microscopy (SEM) at 10 kV acceleration voltage and interpreted (JSM6510LV, Japan; (Selim et al., 2020; Sharaf et al., 2021b).

2.10. Molecular docking

The tridimensional structures of Hesp were downloaded from PubChem (ID 10621; (Kim et al., 2019) and docked onto the urease structure of *H. pylori* ATCC 700392 obtained from PDB (ID 4HI0; (Fong et al., 2013) by using AutoDock Vina (Trott and Olson, 2010). The ligand (Hesp) was considered flexible, and a ligand-specific torsion tree was defined. Furthermore, the protein structure was considered rigid, and a grid enclosing the whole structure of the protein was defined. This grid represented the search space for putative interaction sites. Accordingly, precalculated maps were defined for the ligands. These maps included independent maps for the whole atom in the ligand and integrated desolvation and electrostatic potential. The Auto Grid algorithm was then used in evaluating the interaction energy of a ligand conformation by summing up the contributions of the atoms of a specific element at any point in the grid near the rigid receptor. The docking results

obtained through scanning the search space of the entire protein structure and passing a threshold (ΔG) of <-8.28 kcal mol^{-1} were ranked in accordance with the estimated interaction energy. Thus, the high-ranking conformation for the ligand was selected as the predicted model of interaction. The ADME profiling of Hesp extraction was performed in accordance with a previous work (Daina et al., 2017).

2.11. Interaction of Hesp with the active site of HpUre

A two-dimensional interaction scheme of Hesp with the catalytic site of *HpUre* was created by using Discovery Studio 2019 (Biovia, 2017). The homology model of the conservation score and the electrostatic surface were created using Pymol (version 1.7.4.5; (Mishra et al., 2016). The Ramachandran plot for the predicted model was created with pdbsum (Laskowski, 2009).

2.12. Molecular dynamics simulations

MD simulation was run by using Schrodinger's Desmond module (Bowers et al., 2006; Beura and Chetti, 2020). Free VMD molecular simulation with NAMD software was used as an alternative, and the Desmond system builder tool was used in producing the solved water-soaked system. The TIP3P model was used as the solvent system in the experiment (Mark and Nilsson, 2001). The orthorhombic simulation was a box that generated a minimum distance of 10 Å from the external protein surface under periodic limit conditions. Predefined balancing was performed prior to simulation. MD simulation was conducted for 100 ns at an environmental pressure of 1013 bar and temperature of 300 K, and 1000 frames were stored on the path. By adding reasonable amounts of contradictions, the isosmotic state was preserved after 0.15 M NaCl was added to the simulation panel. Then, the simulation was evaluated by using a simulation interaction diagram in which the protein–ligand RMSD acted as a metric for calculating the average change in the displacement of a group of atoms in relation to a reference frame. It was computed for each and every frame of the trajectory. For frame *x*, the RMSD was analyzed in accordance with the following equation:

$$RMSD_x = \sqrt{\frac{1}{N}\sum_{i=1}^{N} < \left(\left[(tx) - r_i(t_{ref}) \right]^2 \right)}, \quad (3)$$

where *N* is the number of atoms in the atom selection, t_{ref} is the reference time, r^f is the location of the atoms in framework *x* after the superimposition of the reference frames, and *x* is recorded at time t_x. This technique was repeated for each frame of the simulation trajectory.

The protein RMSF is useful in characterizing local changes along the chain of portions. The residue *i* RMSF was analyzed in accordance with the equation.

$$RMSF_i = \sqrt{\frac{1}{T}\sum_{t=1}^{T} < \left[r_i^f(t) - r_i(t_{ref}) \right]^2} \quad (4)$$

where *T* is the trajectory period during which the RMSF is calculated, t_{ref} is the reference period, and r_i is the residue position *i.* r^f is the atom location *i* after overlapping on the reference, and the angle brackets indicate that the average square distance is taken over the residue's atom selection. Protein–ligand contacts, ligand–protein contacts, and torsion profiles were analyzed.

2.13. Statistical analysis

The output of statistical analysis was depicted as mean ± SEM, and the experimentally collected data were statistically analyzed through one-way ANOVA. $^*P < 0.05$,$^{**}P < 0.01$, and$^{***}P < 0.001$ were considered significant differences when compared with the control. Graphpad Prism 8.0.2 (San Diego, CA, USA) was used in evaluating statistical results.

3. Result and discussion

3.1. Evaluation of Hesp purity

An HPLC array detection system was used in analyzing Hesp purity. The results are summarized in Fig. S3. The HPLC chromatogram revealed that the Hesp standard and the isolated Hesp had retention times of 2.687 and 2.740 min, respectively. The content of pure Hesp in the crude extract of citrus peel was 95.14 μg mg^{-1} of dry raw material (Fig. S3B). Impurities showed high absorption at approximately 285 nm and similar spectra. Nine flavonoid compounds were identified at extremely low ratios that were almost nonexistent when compared with the Hesp standard (Fig. S3A) and were not pharmacological impurities. Hence, these flavonoid impurities might have been generated after the use of a different extraction method. These results were closely similar to previously reported findings (Adham, 2015).

3.2. Characterization of crystalline Hesp status

The results for crystalline Hesp status are shown in Fig. 1 and S4. XRD analysis indicated that the Hesp extracted from *C. uranium* peel showed superimposable diffraction and had the same crystallinity grade as the Hesp standard. Hesp displayed strong characteristic peaks at 2θ values of 7.8°, 11.4°, 15.5°, 17.1°, 19.5°, 22.2°, 23.2°, 25.5°, and 29.1°, which were indicative of its highly crystalline structure (Fig. S4A). These results were similar to previously reported results (Gao et al., 2014; Ali et al., 2019).

As shown in Fig. 1A, the FT-IR spectra of Hesp exhibited characteristic absorption bands at 3605 cm^{-1} (O–H str.), 2895 cm^{-1} (C–H str. alkane), 2297 cm^{-1} (C–H str), 1675 cm^{-1} (alkane–OCH_3), and 1592 cm^{-1} (C=O str.). In addition, an adequate structure-specific understanding of the complex formation of Hesp extracted from citrus peel with molecular-level resolution was obtained through ^{1}H-NMR. The results are summarized in Table S1. ^{1}H-NMR revealed the following chemical shifts in ppm (Figs. 1B and S4B): A δ, 6.93 (H2′, 5′, 6′, H6) benzene cycles; δ 6.13 (H6, 8); δ 5.49 (H2); and δ 3.77 (OCH_3). These finding were similar to the target peaks that were assigned in accordance with reported data (Aghel et al., 2008; Shi et al., 2008; Maltese et al., 2009). Hesp complex formation can be initially attributed to the chemical shift changes (Δδ) of natural products in 10% DMSO-d6 and was consistent with that in D2O in ^{1}H-NMR experiments (Cao et al., 2015). The DSC curves or thermograms exhibited an endothermic peak at 118.5 °C (Fig. 1D).

3.3. Urease inhibition assay

As illustrated in Fig. 2, the reaction mixture was supplemented with different concentrations of Hesp to explore the effect of potential inhibitors on urease activity. Urease inhibition by Hesp led to a progressive reduction in activity. Fig. 2A shows the concentration-dependent activities toward JBU. The residual activity values were obtained as the percentage of the control activity of increasing concentrations of Hesp (0–120 mM mL^{-1}). These findings proved that the OH groups present in the Hesp structure enhanced the interaction of the two successive OH– groups of Hesp with the active site residues of the *JBU* enzyme through hydrogen bonds and thus prevented substrate binding. These effects can be attenuated by increasing substrate concentration to a particular level until the enzyme became saturated and its active site became occupied by the substrate (Yu et al., 2015).

3.4. Kinetic parameters of urease activity and the half-maximal inhibitory concentration of urease

HpUre inhibition is essential to the exploration of effective drugs for

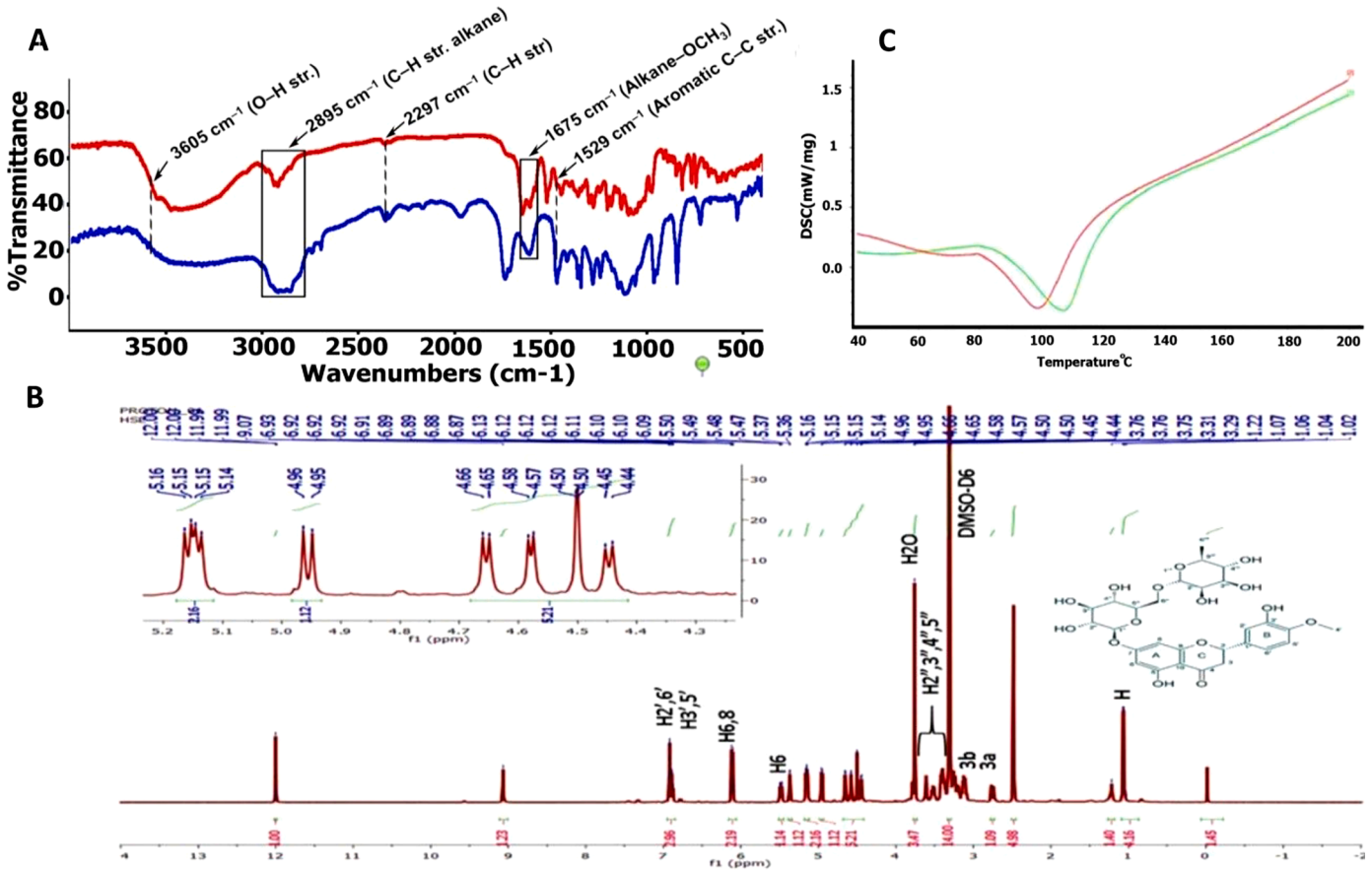

Fig. 1. Crystalline status of Hesp; (A) FT-IR spectra; (B) ^{1}H-NMR spectra (δ, 2.5–7.5 ppm) of Hesp extracted in 10% DMSO-d6 at 25°C; and (C) DSC curves/thermograms.

various pathophysiological conditions, such as oxidative stress, gastritis, peptic ulcers, and gastric cancer urease-positive pathogens (Katarzyna, 2013). The urease activity of soluble Hesp was assayed by using a colorimetric technique for ammonia formation quantification. The kinetic properties of urease were determined in different concentrations of urea (0.163–20 mM). A detailed kinetic analysis of the inhibitory effect of the *JBU* enzyme on urea in the absence and presence of Hesp is summarized in Table 1. The enzyme yielded a simple Lineweaver–Burke plot with a linearized double reciprocal (Fig. 2B) and a standard hyperbolic Michaelis–Menten plot (Fig. 2C). The kinetics values of the enzyme were indicative of competitive inhibition and showed a noticeable increase in *Km* and an almost identical V_{max} (Table 1). Furthermore, the half-maximal inhibitory concentration (IC_{50}) of Hesp was approximately 40.6 mM ($logIC_{50}$), whereas that of the standard urease inhibitor (thiourea acid) was 23.4 mM ($logIC_{50}$; Fig. 2D). The inhibitory constant K_i reflects the concentration required to half activity. The K_i calculated from the Lineweaver–Burke plots for Hesp was 27.8 μM (Table 1)

3.5. Antimicrobial properties

3.5.1. LSCM analysis

The viability and architecture of bacterial cells were investigated through LSM to determine the eradication efficiency of Hesp for *H. pylori* ATCC 700392 the results are shown in Fig. 3. SYTO 9 is a green fluorescent dye that binds to viable and stable bacteria, and PI is a membrane-impermeable dye that is usually applied to stain cells with destroyed or damaged membranes; the emission of red fluorescence indicates dead cells (Figs. 3B–K; (Kang et al., 2007). The untreated bacterial group (control) showed a compact architecture and comprised a large number of live cells with intense green fluorescence (Figs. 3A and C). The bacterial groups treated with different concentrations of Hesp exhibited a favorable relationship between the extent of *H. pylori* strain disruption and the concentration of Hesp. *H. pylori* was destroyed at varying degrees. No apparent dead cells were detected. Bacterial viability exceeded 85.3% after treatment with 150 μg mL^{-1} free Hesp, which was unable to kill *H. pylori* effectively (Figs.3D and F).

However, the bacterial group treated with 250 μg mL^{-1} Hesp exhibited an apparent reduction in green fluorescence signals and increase in red fluorescence signals compared with the untreated bacteria, which showed reduced susceptibility to antimicrobial drugs resistance and viability exceeding 60.5% (Figs. 3G and I).

Additionally, only a small number of dead cells were detected when the bacteria were treated with Hesp at specific concentrations. In particular, bacterial viability was less than 30.7% after treatment with 500 μg mL^{-1} HESP (Figs. 3J and L) likely because the initial damage caused by Hesp to the *H. pylori* lipid membrane accelerated the killing of the *H. pylori* strain and increased the bacteria's permeability to external fluids.

The anti-*H. pylori* effects for flavonoids vary according to the molecular structure of the compound. Hence, our results regarding the effects of Hesp on *H. pylori* ATCC 700392 urease inhibition can be attributed to the minor difference in chemical structure among flavonoids, such as hesperetin (González et al., 2019; Kim et al., 2021), quercetin, and apigenin, which might be responsible for varied effectiveness in their capacity to inhibit the biological activity of the same protein target. where both apigenin and quercetin enabled to hinder D-alanine ligase (Ddl) action by using the same inhibitory mechanism as that competing with the substrate ATP (Wu et al., 2008). The only difference between the two compounds is that quercetin has two additional

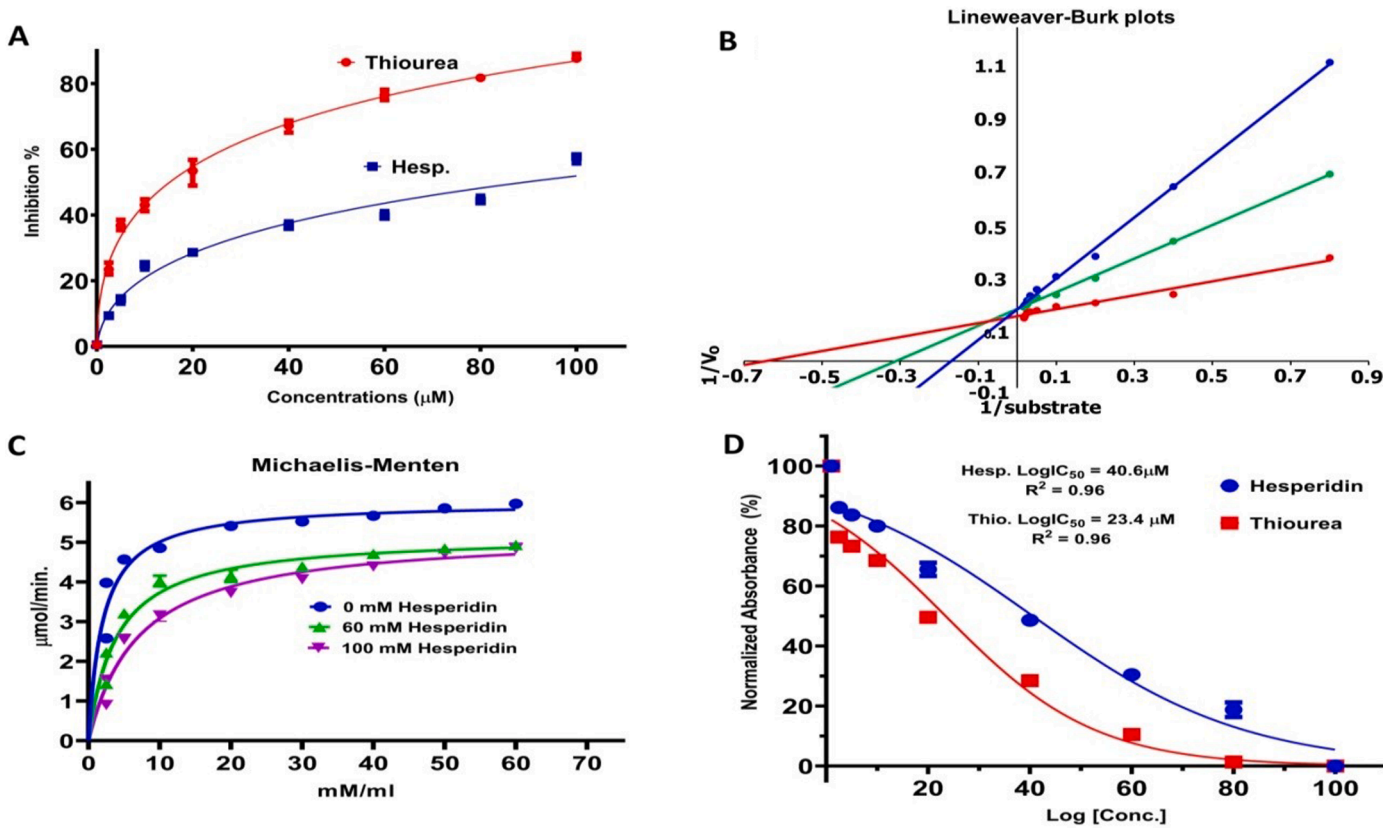

Fig. 2. (A) Urease inhibition curves of *JBU* urease activity as a function of Hesp and standard urease inhibitor concentration (thiourea); (B and C) double-reciprocal Lineweaver–Burke plot and Michaelis–Menten plot of the reaction rates vs. the reciprocal of urea concentration in the reaction mixture in the absence of Hesp and in the presence of 60 and 100 mM Hesp; (D) IC_{50} of pure urease inhibition by Hesp at different concentrations and the standard urease inhibitor. Results are shown as the means ± SD of three independent tests.

Table 1
Kinetic analysis constant values (*Km*) and maximum velocity (V_{max}) values of *JBU* at different concentrations of the inhibitor Hesp and urea substrate.

Optimize and kinetic values for enzyme activity		IC_{50} (μM)		Binding affinity (△G, kcal mol^{-1})	Ki (μM)	Type of inhibition
pH	7.0	Hesp	40.6	−8.28	27.8	Competitive
Temp.	37°C	Thiourea	23.4			
Reaction time	10 min					
Hesp. conc.	**Michaelis–Menten**		**Lineweaver–Burke plots**			
	V_{max} (U mg^{-1})	*Km* (mM mL^{-1})	V_{max} (U mg^{-})	*Km* (mM mL^{-1})		
0 mM	6.1 ± 0.12	1.2 ± 0.23	5.89 ± 0.82	1.5 ± 0.16		
60 mM	5.2 ± 0.11	3.9 ± 0.37	5.09 ± 0.56	3.2 ± 0.14		
100 mM	5.2 ± 0.13	7 ± 0.64	5.12 ± 0.53	5.9 ± 0.72		

hydroxyl groups at positions 3 and 3′. This small difference causes a significant increase in quercetin's affinity for the active site of an enzyme, resulting in a threefold increase in its inhibitory activity against Ddl. Quercetin showed lower antibacterial activity than apigenin possibly because of poor transport across the bacterial cell membrane with reduced lipophilicity (Wu et al., 2008). Bergamot juice with 167.5 mg L^{-1} Hesp and 1.8 mg L^{-1} CLR was the most effective treatment against *H. pylori* clinical isolates *H. pylori* 61 and the cagA-positive strain *H. pylori* 6 (Gardana et al., 2008; Filocamo et al., 2015).

Polysaccharide (LPS) is the main component of the outer membrane of *H. pylori* (Zgurskaya et al., 2015). FITC can bind explicitly to D-(+)-glucose and D-(+)-mannose LPS groups. The strains that had been incubated for 30 min with different concentrations of Hesp were compared with the control group. The absence of green fluorescent spots in the control sample indicated that the bacterial cells were stable and viable (Fig. 4A). The green fluorescent spots in Figs. 4B–D indicated that FITC had been increasingly internalized in the outer membrane of *H. pylori* cells and accumulated in vacuoles by binding with the LPS receptor and conjugation with the damaged cell membrane. Increase in Hesp concentrations caused bacterial membrane disruption and cell death, as demonstrated by FITC staining (Li et al., 2013; Arif et al., 2021a).

3.5.2. SEM

SEM revealed that Hesp caused extensive morphological changes and exerted bactericidal effects against *H. pylori* ATCC 700392. The antimicrobial effects of Hesp on the morphology of the tested bacterial strains were explored in untreated *H. pylori* ATCC 700392 (PBS) and cultures treated with 125, 250, and 500 μg mL^{-1} Hesp through SEM. The results are shown in Fig. 5.

SEM revealed that the untreated *H. pylori* ATCC 700392 (control) cells increased in number, aggregated, had smooth and intact cell membranes, and underwent binary or multiple fission after 12 and 24 h (as indicated by the blue outlined arrows in Figs. 5A and B). SEM images illustrating the time course of the *H. pylori* ATCC 700392 culture treated

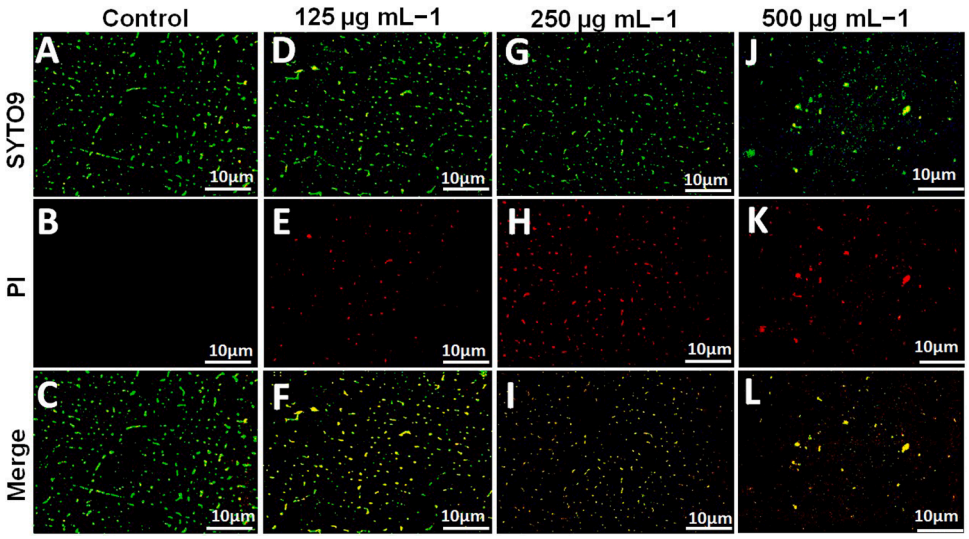

Fig. 3. Live (green): dead (red) fluorescence ratio of *H. pylori* ATCC 700392 exposed for 24 h to different treatments; (A and C) *H. pylori* treated PBS of control; (D and F) *H. pylori* treated with 125 μg mL^{-1} Hesp; (G and I) *H. pylori* treated with 250 μg mL^{-1} Hesp; and (J and L) *H. pylori* treated with 500 μg mL^{-1} Hesp (scale bar = 10 μm).

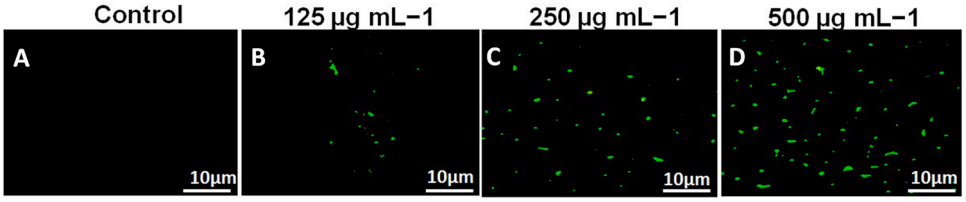

Fig. 4. Intracellular protein release of FITC; (A) untreated cells displaying no fluorescence (control); (B–D) intracellular protein leakage analysis of the *H. pylori* strain ATCC 700392 treated with 125, 250, or 500 μg mL^{-1} of Hesp. The green fluorescent spots indicated that FITC had been increasingly internalized in the outer membrane of the *H. pylori* cells.

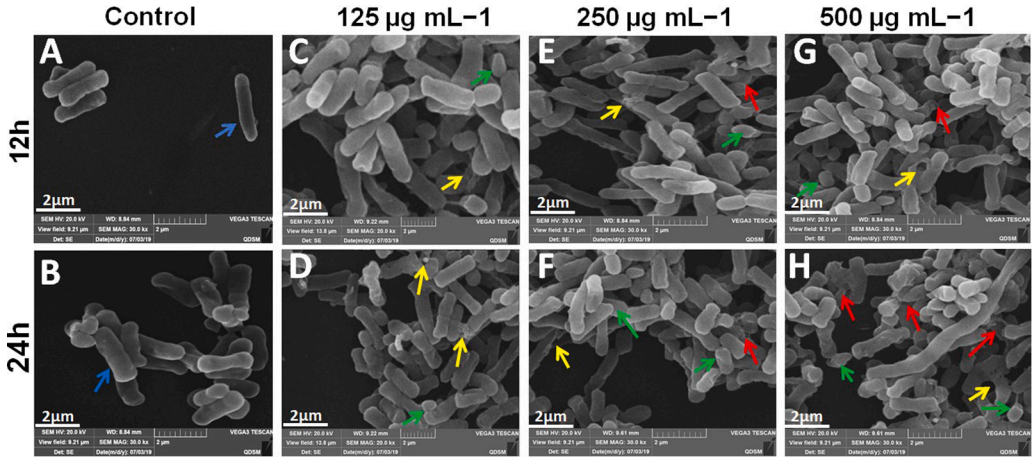

Fig. 5. SEM images of *H. pylori* ATCC 700392 after 12 and 24 h of exposure to different treatments: (A and B) *H. pylori* treated with PBS of control; (C and D) *H. pylori* treated with125 μg mL^{-1} Hesp; (E and F) *H. pylori* treated with 250 μg mL^{-1} Hesp; and (G and H) *H. pylori* treated with 500 μg mL^{-1} Hesp (scale bar = 2 μm). Blue arrows show smooth and intact cell membranes, yellow arrows designate underwent some morphological changes and membrane damage, green arrows indicate the shrinkage and protrusion of some bacterial cells, and red arrows show rupture and bacterial death.

with pure Hesp showed that Hesp had a distinct effect after 12 and 24 h of treatment (Figs. 5 C-H).

The yellow outlined arrows in Figs. 5C and D indicated that the *H. pylori* strain treated with 125 μg mL^{-1} Hesp underwent some morphological changes after 12 and 24 h of incubation. Holes and rupture were found in the outer membrane, some biological processes were suppressed, and some bacterial cells shrank (green outlined arrows; (Seabra et al., 2017; Yan et al., 2022). As a result, lipophilic flavonoids, such as herperetin, naringenin, sophoraflavanone G, and catechins with gallate groups, penetrated the lipid bilayer up to the phosphate group zone and laterally diffused into the bilayer plane, altering membrane fluidity and permeability (Tarahovsky et al., 2014).

Furthermore, SEM images illustrated morphological changes in most treated *H. pylori* strains after 12 and 24 h of incubation with 250 μg mL^{-1} pure Hesp. Initial exposure to Hesp resulted in the extensive collapse of the surfaces of bacterial cells and clearly reduced cell growth, as indicated by the red outlined arrows in Figs. 5E and F. A similar effect was observed after 12 and 24 h of incubation with 500 μg mL^{-1} Hesp. Hesp treatment resulted in extensive deterioration, morphological changes, and lethal effects compared with the control treatment. The interaction

of the bacterial cell surfaces with 500 μg mL^{-1} Hesp resulted in cell damage, shriveling, and truncation that subsequently led to severe cell membrane lesion formation, rupture, and bacterial death, as indicated by the red and yellow outlined arrows in Figs. 5G and H. Antibacterial and natural compounds produced from plants can be used to treat *H. pylori* and have the added benefits of low cytotoxicity and minimal side effects (Khan et al., 2021). As previously mentioned by (Moon et al., 2013), Hesp tends to destroy the cell membrane, causing bacterial lysis. Sharaf et al. investigated the role of Hesp in blocking the activity of the *HpUre* enzyme and preventing the normal growth of *H. pylori*. Hesp might first induce the breakdown or disruption of the lipid membrane of *H. pylori* ATCC 700392 (Sharaf et al., 2021a). This effect would enhance the permeability of the bacteria to antibiotics and promote the leakage of intracellular content, consequently causing bacterial death. Kim, Woo et al. found that decreases in the expression levels of *Ure*A and *Ure*B after hesperetin administration reduce the urease activity of *H. pylori* and thereby downregulate the urease subunit, rendering the bacterium unable to convert urea to ammonia and bicarbonate (Kim et al., 2021). This effect may contribute to the inhibition of the initial colonization of *H. pylori* in the stomach and its survival in a highly acidic environment (Hajialyani et al., 2019). Moreover, this effect reduces the number of viable cells and increases the number of damaged dead cells, thus inhibiting urease activity (Azevedo et al., 2007).

Hesp causes significant membrane degradation and destroys membrane integrity. These effects likely involve the perturbation or inhibition of metabolic pathways, such as nucleic acid synthesis, cytoplasmic membrane function, and energy metabolism, and cause cell damage, followed by changes in some of the morphological features of bacteria (Cushnie and Lamb, 2005; Becker-Ritt et al., 2007; Shin et al., 2007). Bartoszewski,G et al. mentioned that flavonoids may interact with proteins, such as adhesins, enzymes, and toxins, which are involved in various essential functions at the membrane surface and in the cytosol and inactivate these biomolecules by forming flavonoid–protein complexes through hydrophobic interactions and hydrogen and covalent bonds (Górniak et al., 2019).

3.6. Molecular docking and interaction of Hesp with the active site of HpUre

No published reports have described the urease–ligand (Hesp) structure. Thus, this work aimed to gain further insight into the working molecular mechanism of the inhibitory effect of Hesp (ligand) on *HpUre*. The results are shown in Fig. 6. The *HpUre* enzyme (PDB ID 4HI0) consists of 11 α-helixes and 7 β-strands arranged in a parallel fashion. The molecular docking of possible interactions was carried out by using Autodock tools, and the preferable possible binding modes of the

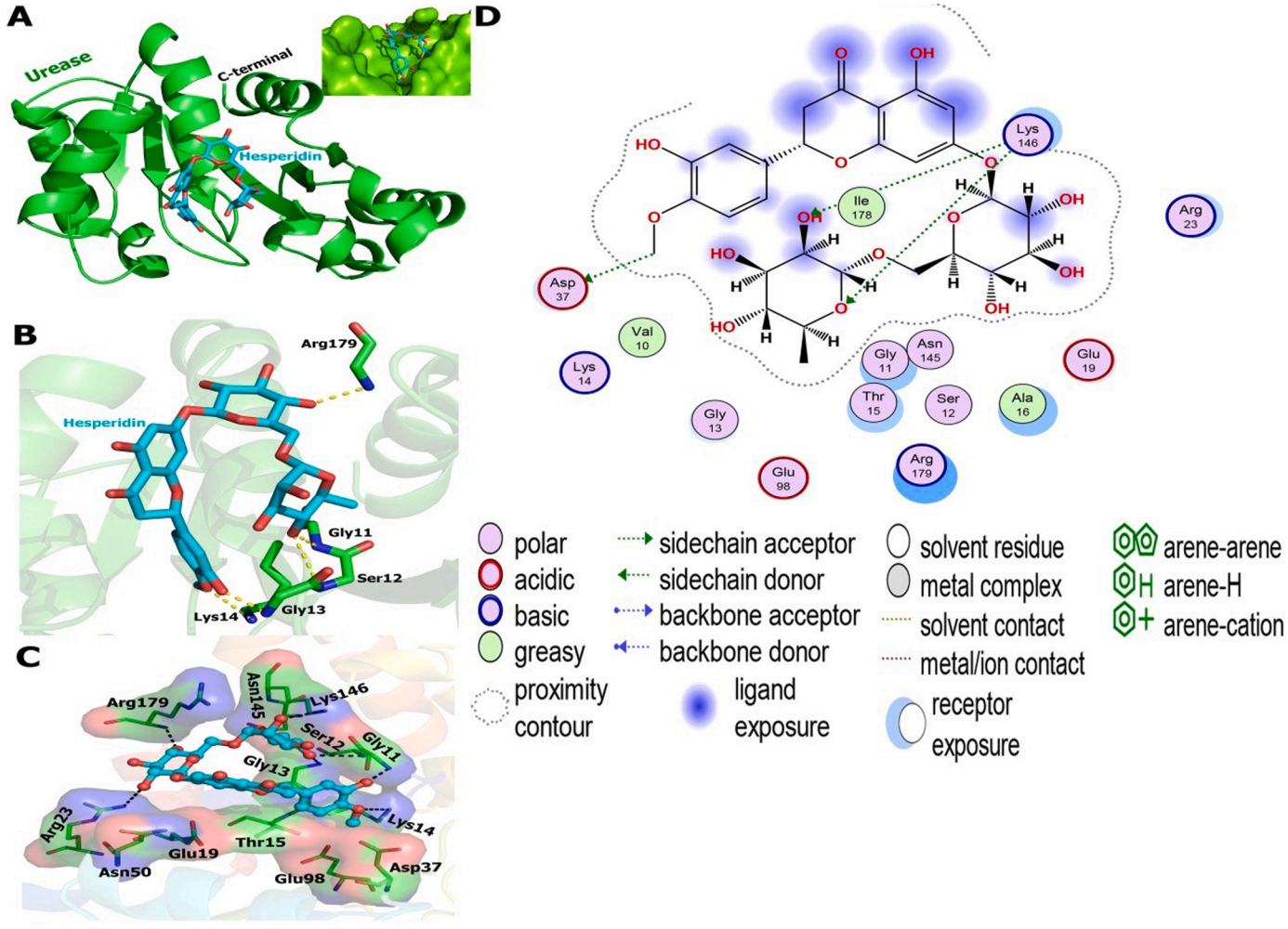

Fig. 6. Molecular docking simulations from the lowest energy conformation. (A) Surface depiction of the urease's active-site flap with the ligand near the binding pocket's entrance. (B) Amino acids involved in the hydrogen bonds of the ligand are shown as sticks. These figures were created by PyMol. **Notes**: the ligand is in cyan, the crystal structure of *HpUre* (PDB ID 4HI0) is in green; oxygen atoms are colored red; nitrogen atoms are in blue; and yellow dashes refer to bonding interactions. (C) van der Waals and alkyl interactions with the residues of the catalytic site that are crucial to the inactivation of the enzyme. (D) Electrostatic surface of *HpUre*. Positive charges are highlighted in blue; negative charges, in red; and neutral charges, in white.

HpUre–ligand are shown in cartoon mode (Fig. 6A). The amino acids involved in hydrogen bonds were Gly11 (O···H distance = 2.2 Å), Gly13 (O···H distance = 2.4 Å), Ser12 (O···H distance = 3.3 Å), Lys14 (O···H distance = 3.3 Å), and Arg179 (O···H distance = 2.7 Å) (Fig. 6B). Val10, Thr15, Ala16, Asp37, and 145, Glu98, Lys146, and Iso178 were involved in hydrophobic interactions that stabilized ligand binding. Moreover, the full fitness and the logarithm of free binding energy (△G) of urease to the ligand active site in the docked conformation were −1220.23 and −8.28 kcal mol^{-1}, respectively.

The ligand exerts its anti- *H. pylori* activity by inhibiting *HpUre*. The molecular docking study clearly demonstrated that the ligand bound to the active site of urease through hydrogen bonding (Gly11 and 13, Ser12, Lys14, and Arg179) and hydrophobic interactions (Val10, Thr15, Ala16, Asp37 and 145, Glu98, Lys146, and Iso178). We believe that these amino acids contribute to the acceleration of reactions and stabilized catalytic transition state by restricting the accessibility of the active catalytic conformation of urease.

Furthermore, the obtained results indicated that the ligand interacted with the active site of *HpUre* by establishing hydrogen bonding, van der Waals, and alkyl interactions with the important residues of *HpUre* active sites (Fig. 6C). These interactions are crucial to the suppression of *HpUre* activity. Interestingly, the ligand was found to bind to the same active pocket of the enzyme and interacted with guanosine-5′-diphosphate active sites. These features indicated that the ligand competed with the substrate and thus acted as a competitive inhibitor by creating enzyme–product complexes.

Additionally, docking scores (expressed as binding affinities) for the ligand and *HpUre* were obtained, and the results are shown in Fig. 6D. The predicted *HpUre* and ligand model was found to be reasonable and reliable for *in silico* docking studies. Furthermore, *HpUre* had highly and lowly conserved amino acids on its active site surface. This feature is what distinguishes *HpUre* from other *HpUre* molecules. Ligand binding motifs were apparent in these conserved amino acids. Therefore, the binding motifs were identified as the conserved surface residues involved in dimer formation. All residues were present within the permitted areas. The *in silico* docking studies showed that the positive and natural electrostatic areas were the two electrostatic houses of the active site given that half of the ligand locus was in the positively charged area, whereas the other half was found in the natural electrostatic area (Fig. 6D).

The bioavailability of Hesp is linked to its physicochemical properties. Drug development is hindered because of the poor pharmacokinetic and safety profiles of new chemical entity (Chen et al., 2018). Many computational approach can help us predict the drug-likeness activity and potential toxicity of novel compounds in the initial phases of drug discovery. Hesp has high activity potential, as presented in Fig. S5A, which shows that Hesp met all the criteria for oral use. The physicochemical, pharmacokinetics, and drug-likeness properties of potent hits were as follows: bioavailability source, 0.17; Ghose, no; TPSA, 234.29 $Å^2$; water solubility, −3.28 soluble; BBB permeant, no; P-gp substrate, yes; and CYP isoform interacts, no. These results showed that Hesp is water soluble, does not cross the blood–brain barrier, interacts with the major enzyme cytochrome P450, and has P-gp substrate properties.

Ramachandran plots were used in determining the accuracy of the results. A total of 197 (100%) total residues were found in the permitted area, whereas no other residues were found in large quantities in the disallowed region. G-factors are the indicators of abnormal stereochemical property. Values below −1.0 represent high abnormality, and values below −0.5 indicate an odd property. The G-factors for covalent forces in the main chain and dihedral angles were approximately 0.5. The backbone dihedral angles, phi, and psi in the 3D model were within permissible limits in accordance with the Ramachandran plot and G-factors based on PROCHECK, RMSD, and ProSA program findings (Fig. S5B).

3.7. MD simulations

3.7.1. Protein root mean square deviation and protein root mean square fluctuation

The inhibition of *HpUre* by the ligands was determined through the MD simulation of the protein–ligand complexes and through multiple dynamic trajectory studies (RMSD and RMSF). The findings are presented in Fig. 7.

The RMSD development of a protein (left Y-axis) is illustrated in Fig. 7A. The RMSD was determined in accordance with atom assortment after all the protein frames were aligned to the reference frame backbone. The RMSD of a protein provided insight into the protein's structural conformation throughout the simulation. When MD simulation is equilibrated, RMSD analysis can show that the oscillations near the conclusion of the simulation may be attributed to a thermal average structure. In small globular proteins, changes on the order of 1.00–3.00 Å are entirely acceptable. Large changes imply that a protein undergoes considerable conformational shifts throughout the MD simulation (ns). In MD simulations, convergence is crucial, that is, RMSD values should be nearly equal to a constant number. The system is not in equilibrium when the RMSD of a protein is increasing or decreasing after MD simulation. Thus, the duration of the MD simulation may be insufficient for robust analysis.

Furthermore, as compared with that of the initial model of Hesp throughout the 1000.0 ns time scale plot, the protein RMSD trajectory of the Cα atoms in the *HpUre*–ligand complex increased until 8.00 ns of MD simulation and then progressively tended to equilibrate after 11.0 ns during the simulation trajectory (0.00–100.05 ns). The RMSD average value of the Cα atoms in the *HpUre*–ligand complex after equilibrium was 1.5 Å.

A thorough study of the RMSF profile of the *HpUre* protein bound to the ligand molecule revealed fluctuations in the amino acids in the urease sequence. The maximum fluctuation was approximately 6.40 Å at 300 residue index position in the protein chain.

The resultant RMSF profile presented fluctuations in a range of 1–2 nm at the active sites of the *HpUre* protein of the Hesp ligand. No fluctuations were observed at the active sites in the *HpUre*–ligand complex. A high level of mobility with fluctuations between 4 and 25 nm were observed at the noncatalytic sites. This factor was not considered significant in the current study given that we focused on the dynamic behavior of the active site of *HpUre* (Fig. 7B).

3.7.2. Ligand torsion profile

The ligand torsion histogram depicting the structural evolution of each rotatable bond (RB) in the ligand during the simulation trajectory (0.00 ns to 100.05 n) is shown in Figs. 8A, B, and C. The two-dimensional structure of the ligand with a color-coded RB is displayed, and a radial plot and a bar plot with similar color coding are accompanied by each RB torsion (Fig. 8A). The dial (or radial) graphs describe torsional conformation during the simulation. The ligand was flexible in the allosteric site, and the torsional rotations of the –OH side groups of the ligand were observed along the simulation trajectory. These results may provide insights into the conformational strain that retains the protein-bound shape of a ligand (Fig. 8B).

3.7.3. Ligand properties

As shown in Fig. 8C, the studied ligand properties included the RMSD ligand, radius gyration (rGyr), the molecular surface area (MolSA), solvent-accessible surface area (SASA), and the polar superface area (PSA).

The RMSD varied until 100 ns and then progressively balanced. The RSMD of the ligand with respect to the conformation of the reference (the type of the first frame was referred to as time t = 0.00) ranged from 1.00 Å to 3.00 Å, and its balance was approximately 2.25 Å. The rGyr is the radial distance to a site where the actual mass distribution (ligand) occurs at the same moment of inertia when the total body (ligand) mass

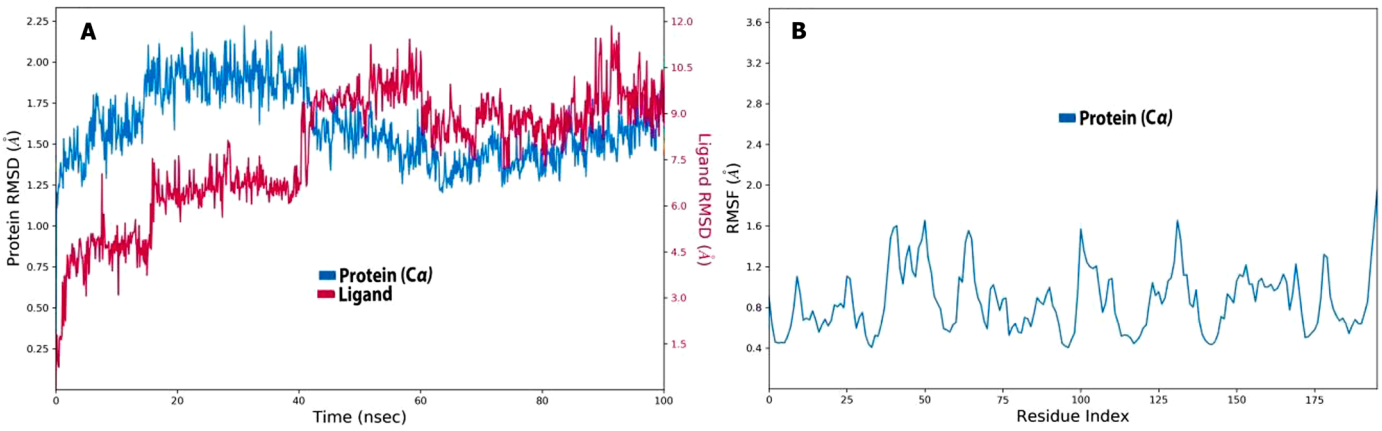

Fig. 7. (A) RMSD plot obtained for (Hesp) of the protein–ligand *HpUre* complexes: protein Cα and compound RMSD shown in blue and red color, respectively; (B) RMSF plot of the protein's backbone atoms during the 100 ns MD simulation: protein Cα RMSD shown in blue.

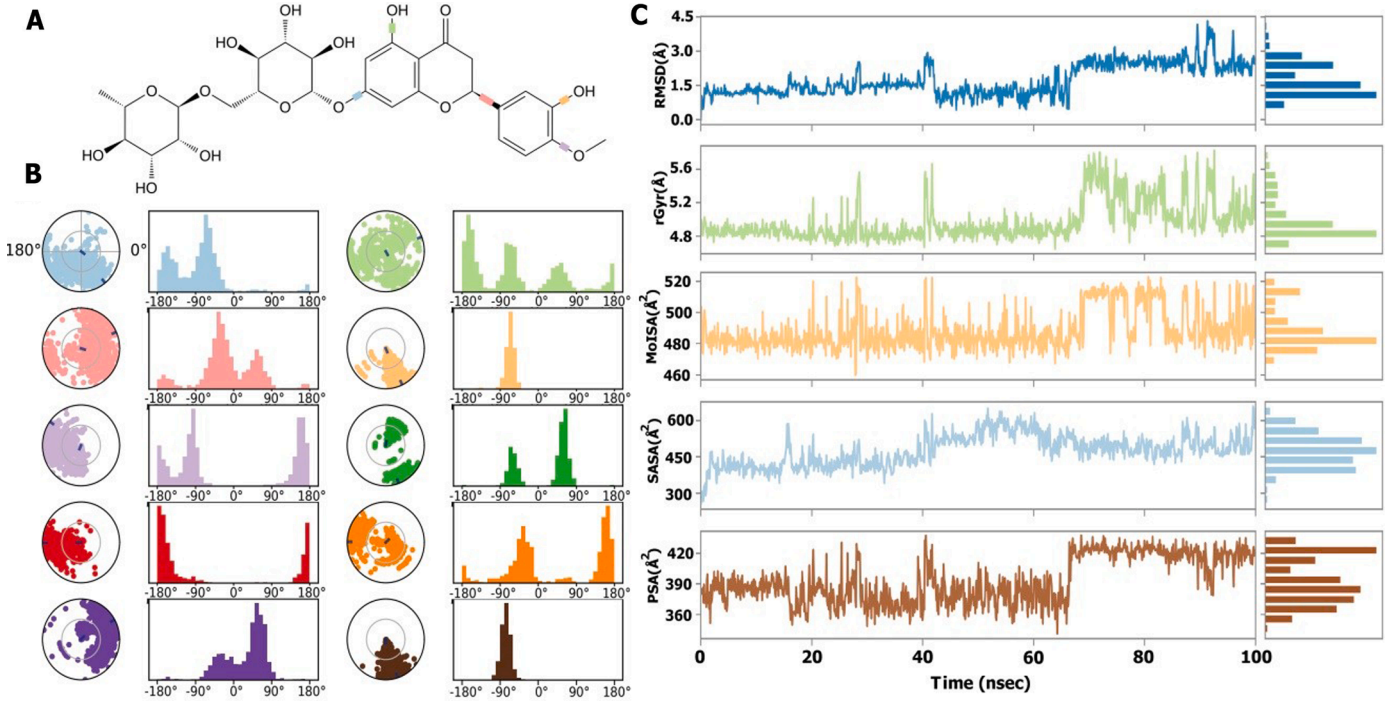

Fig. 8. Ligand torsion profile (A) torsion and flexibility; (B) ligand torsion angles; and (C) ligand (Hesp) property trajectory of the ligand–*HpUre* complex: the ligand properties fluctuate during the begining or intermediate simulation periods, but gradually return to equilibrium during 100 ns of simulation, indicating that ligand is stable at the active site of the protein.

is concentrated. Ligand extension was measured on the basis of rGyr, which corresponds to the primary moment of inertia. The rGyr considerably varied in the ligand up until 65.00 ns of the simulation period and ranged from 4.8 Å^2 to 5.00 Å^2. The MolSA was calculated using a probe with a radius of 1.400 Å. This number was comparable to the van der Waals surface. The MolSA ligand changed constantly during the simulation. MolSA values for the ligands ranged from 460 Å^2 to 520 Å^2. The SASA is the surface area of an aquatic molecule. The SASA of the *HpUre*–Hesp ligand complex greatly varied up until 40.00 ns of the MD simulation and then gradually stabilized. It ranged from 300 Å^2 to 600 Å^2 and reached equilibrium at approximately 450 Å^2. The PSA refers to a molecule's solvent-accessible surface area, which is contributed by oxygen and nitrogen atoms only. The ligand's PSA fluctuated at a consistent rate throughout the simulation. The PSA values of the ligand varied from 360 Å^2 to 420 Å^2. Finally, all the ligand characteristics fluctuated throughout the initial simulation period or over the simulation period but gradually reached equilibrium at the end of the simulation. This behavior indicated that the ligand was stable at the active site of the protein.

3.7.4. *HpUre protein–ligand contacts*

The stable ligand–receptor *HpUre*–Hesp complex was studied using the protein–ligand contact histogram with terms categorized into four types: hydrogen bonds, hydrophobic, ionic, and water bridge (Figs. 9A, B, and C; (Dariya and Nagaraju, 2020).

In drug design, hydrogen bonds have an important role in ligand binding and a substantial effect on drug selectivity, metabolism, and adsorption. During the MD simulations, *HpUre–Hesp* complex interactions across the hydrogen bonds increased, whereas the average total energy decreased (Figs. 9A and B). The current *in silico* study showed that the Hesp docking conformation can adapt an hydrogen bond and an appropriate orientation with the binding pocket residues of

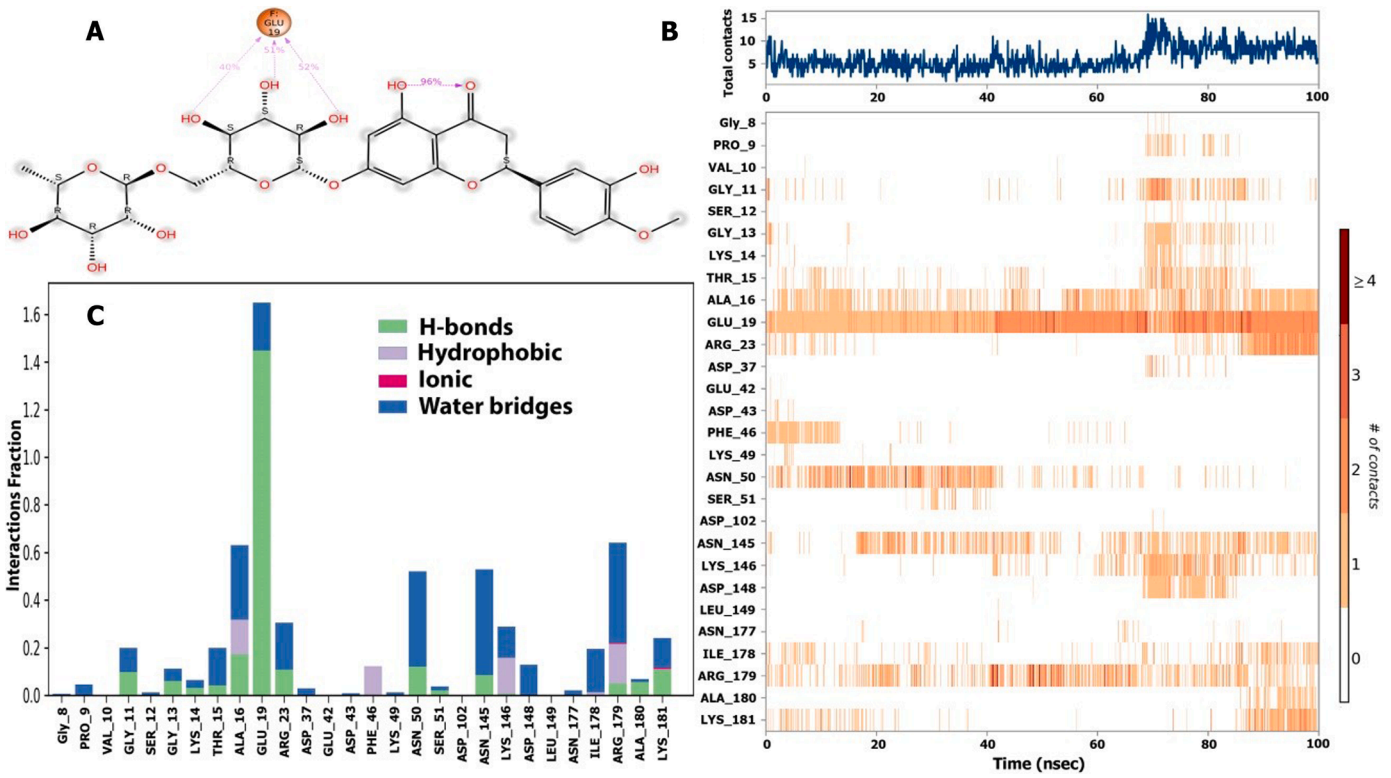

Fig. 9. Diagram of the interaction of Hesp with the *HpUre* protein. (A) Schematic of the interaction of the ligand–protein amino acid residue complexes through hydrophobic interactions, hydrogen bonds during MD simulation; (B) protein–ligand contact plots and interaction residues for the (Hesp) complexes; and (C) residues that interact with the ligand in each trajectory frame. Residues that interact with the ligand in each trajectory frame: Hydrogen bindings (H-bonds) are playing a crucial role in protein folding, protein-ligand interactions.

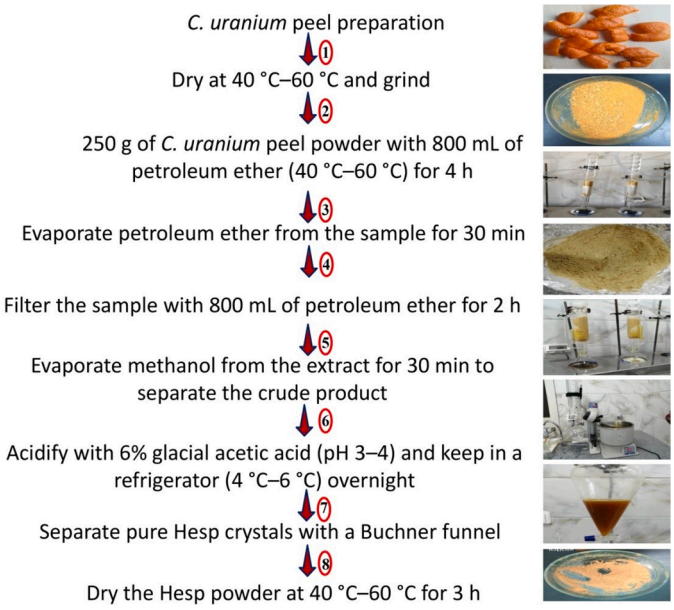

Scheme 1. Preparation and extraction of *C. uranium* peel and separation of Hesp.

HpUre. The active sites of amino acids (Gly11, Gly13, Lys14, Thr15, Ala16, Glu19, Arg23, Asn50, Ser51, Asn145, Arg179, Ala180, and Lys181) interacted through hydrogen bonds (Fig. 9B).

Ionic interactions occur when two oppositely charged atoms are within 3.7Å of each another and no hydrogen bond exists between them. The results showed that Arg179 and Lys181 had minimal ionic interactions with the ligand. Moreover, the hydrophobic contact points of amino acids (namely, Ala16, Phe46, Lys146, Ile178, and Arg179) interacted with the aromatic or aliphatic group on the ligand (Fig. 9B).

Water bridges reflect the interactions between H-bonded proteins and the ligand (Hesp) mediated by a water molecule. The current geometric criteria for a protein–water or water–ligand hydrogen bond are as follows: distance of 2.8 Å between donor and acceptor atoms (D—H….. A); donor angle of ≥110°; and acceptor angle of ≥90 between the donor–hydrogen-acceptor atoms (D—H….A) and the hydrogen-acceptor-bonded atom (H….A—X).

The geometry of the hydrogen bond was slightly relaxed relative to that of the standard hydrogen bond. Almost all the major interacting amino acids had water bridges, except two amino acids, namely, Ala16 and Pro352, which accounted for approximately 27% and 86% of the highly effective interactions of the protein–ligand complex time interactions (100 ns simulation), respectively.

The protein–ligand contacts were described using a ligand–receptor interaction histogram (Fig. 9C). Fig. 9C displays the total number of individual interactions between a protein and a ligand throughout trajectory. The number of interactions changed from 0.00 Å to 4.00 Å above the sequence of the trajectory curve. The contribution of the amino acids in each trajectory frame of a 100 ns MD simulation was investigated. The scale below the figure shows that some residues made more than one specific contact with the ligand in a given trajectory frame, as indicated by the deep orange color. The *HpUre* receptor–ligand complex exhibited deep orange bands (Glu19, Asn50, Asn145, and Arg179 rows), indicating that the aforementioned amino acid had strong interactions with the ligands in virtually all conceivable orientations (geometry). These results matched the histogram data precisely.

4. Conclusions

By using molecular docking and MD simulation, we showed for the first time that Hesp had a strong inhibitory effect on *HpUre* through slow-binding inhibition, the formation of hydrogen bonding interactions with the active pocket residues and molecular interactions of target proteins. Our findings revealed that Hesp can be derived from citrus peel with a purity of 95.14 μg mg^{-1} of dry raw material *in vitro*. XRD, ^{1}H-NMR, FT-IR, and DSC curves or thermograms demonstrated that the crystallinity rating of the extracted Hesp was the same as that of the Hesp standard. Urease inhibition kinetic analysis showed that Hesp acted as an anti- *H. pylori* agent through a robust competitive mode in a time-dependent manner. The bioavailability assay based on the physicochemical properties of the Hesp molecule revealed that Hesp has high activity potential and satisfies all conditions for oral usage. In addition, LSCM indicated that Hesp treatment causes amino acids to leak from bacterial cells. Moreover, the SEM bioimaging studies illustrated that Hesp interacts with bacterial cells and disrupts cell membranes, causing the leakage of cytoplasmic content. The physicochemical, pharmacokinetics, and drug-likeness properties of potent hits revealed that Hesp is water soluble and has P-gp substrate properties. The MD simulations of the protein–ligand complexes, as evidenced by the detailed study of the dynamic trajectories and hydrogen bond profiles during 10 ns of the simulation, revealed conformational shifts during ligand binding with active site residues. Our research provides prospects for developing reliable and precise anti- *H. pylori* drugs with few side effects from natural sources.

FOOTNOTES

The abbreviations used are as follows: *C. uranium. citrus uranium*; Hesp, hesperidin, *H. pylori, Helicobacter pylori;HpUre, Helicobacter pylori* urease; JBU, jack bean urease; HPLC, high performance liquid chromatography; XRD, x-ray diffractions patterns; RMSF, root mean square fluctuation; FT-IR, Fourier transform infrared spectroscopy; DSC, differential scanning calorimetr;^{1}H-NMR, hydrogen-1nuclear magnetic resonance ; RMSD, root mean square deviation; LSCM, laser scanning confocal microscopy analysis; FITC, fluorescein 5(6)-isothiocyanate; SEM, scanning electron microscopy; Rg, radius of gyration; CFU, colony-forming units; IC_{50}, half-maximal inhibitory concentration; OD, optical density; MD simulations, molecular dynamics simulations; and SD, standard diffusion.

CRediT authorship contribution statement

Mohamed Sharaf: Conceptualization, Funding acquisition, Data curation, Formal analysis, Writing – original draft, Writing – review & editing, Visualization. **Muhammad Arif:** Data curation, Formal analysis. **Hamed I. Hamouda:** Data curation, Formal analysis, Writing – review & editing. **Sohaib Khan:** Writing – original draft, Writing – review & editing. **Mohnad Abdalla:** Data curation, Formal analysis. **Samah Shabana:** Formal analysis, Writing – review & editing. **Hussein. E. Rozan:** Formal analysis, Writing – review & editing. **Tehsin Ullah Khan:** Formal analysis, Writing – review & editing. **Zhe Chi:** Formal analysis, Visualization. **Chenguang Liu:** Visualization, Supervision.

Declaration of Competing Interest

The authors have no conflicts of interest to disclose

Acknowledgments

This study was financed by the Natural Science Foundation of Shandong Province (Grant No. ZR2018MC010), the excellent doctoral scholarship award by the Chinese Scholarship Council, and a full scholarship from the Ministry of Higher Education of Arab Republic of Egypt to Mohamed Sharaf.

Supplementary materials

Supplementary material associated with this article can be found, in the online version, at doi:10.1016/j.crmicr.2021.100103.

References

Abou Baker, D., 2020. Plants against Helicobacter pylori to combat resistance: An ethnopharmacological review. Biotechnology Reports 26, e00470.
Adham, AN., 2015. Qualitative and Quantitative Estimation of Hesperidin in Peel and Juice of Citrus Fruits by RP-HPLC Method Growing in Kurdistan Region/Iraq. International Conference on Harmonization (ICH) 8, 9.
Aghel, N, Ramezani, Z, Beiranvand, S., 2008. Hesperidin from Citrus sinensis cultivated in Dezful, Iran. Pak J Biol Sci 11, 2451–2453.
Ali, SH, Sulaiman, GM, Al-Halbosiy, MM, Jabir, MS, Hameed, AH., 2019. Fabrication of hesperidin nanoparticles loaded by poly lactic co-Glycolic acid for improved therapeutic efficiency and cytotoxicity. Artificial cells, nanomedicine, and biotechnology 47 (1), 378–394.
Amieva, M, Peek Jr, RM., 2016. Pathobiology of Helicobacter pylori–induced gastric cancer. Gastroenterology 150 (1), 64–78.
Arif M, Sharaf M, Samreen, Khan S, Chi Z, Liu C-G. Chitosan-based nanoparticles as delivery-carrier for promising antimicrobial glycolipid biosurfactant to improve the eradication rate of Helicobacter pylori biofilm. Journal of Biomaterials Science, Polymer Edition 2021a:1-19.
Arif M, Sharaf M, Samreen, Dong Q, Wang L, Chi Z, Liu C-G. Bacteria-Targeting Chitosan/Carbon Dots Nanocomposite with Membrane Disruptive Properties Improve Eradication Rate of Helicobacter pylori. Journal of Biomaterials Science, Polymer Edition 2021b (just-accepted):1-19.
Azevedo, NF, Almeida, C, Almeida, C, Cerqueira, L, Dias, S, Keevil, CW, Vieira, MJ., 2007. Coccoid form of Helicobacter pylori as a morphological manifestation of cell adaptation to the environment. Applied and environmental microbiology 73 (10), 3423–3427.
Babu, TMC, Rajesh, SS, Bhaskar, BV, Devi, S, Rammohan, A, Sivaraman, T, Rajendra, W., 2017. Molecular docking, molecular dynamics simulation, biological evaluation and 2D QSAR analysis of flavonoids from Syzygium alternifolium as potent anti-Helicobacter pylori agents. RSC advances 7 (30), 18277–18292.
Bae, E-A, Han, MJ, Kim, D-H., 1999. In vitro anti-Helicobacter pylori activity of some flavonoids and their metabolites. Planta medica 65 (05), 442–443.
Basu A, Sarkar A, Maulik U. Computational approach for the design of potential spike protein binding natural compounds in SARS-CoV2. 2020.
Becker-Ritt, A, Martinelli, A, Mitidieri, S, Feder, V, Wassermann, G, Santi, L, Vainstein, M, Oliveira, J, Fiuza, L, Pasquali, G., 2007. Antifungal activity of plant and bacterial ureases. Toxicon 50 (7), 971–983.
Beura, S, Chetti, P., 2020. Identification of potential human COX-2 inhibitors using computational modeling and molecular dynamics simulations. Journal of Molecular Structure 1216, 128271.
Biglar, M, Sufi, H, Bagherzadeh, K, Amanlou, M, Mojab, F., 2014. Screening of 20 commonly used Iranian traditional medicinal plants against urease. Iranian journal of pharmaceutical research: IJPR 13 (Suppl), 195.
Biovia DS. Discovery studio modeling environment: Release; 2017.
Bowers, KJ, Chow, DE, Xu, H, Dror, RO, Eastwood, MP, Gregersen, BA, Klepeis, JL, Kolossvary, I, Moraes, MA, Sacerdoti, FD., 2006. Scalable algorithms for molecular dynamics simulations on commodity clusters. SC'06: Proceedings of the 2006 ACM/IEEE Conference on Supercomputing. IEEE, p. 43.
Cai, J, Huang, H, Song, W, Hu, H, Chen, J, Zhang, L, Li, P, Wu, R, Wu, C., 2015. Preparation and evaluation of lipid polymer nanoparticles for eradicating H. pylori biofilm and impairing antibacterial resistance in vitro. International journal of pharmaceutics 495 (2), 728–737.
Caligiani, A, Acquotti, D, Palla, G, Bocchi, V., 2007. Identification and quantification of the main organic components of vinegars by high resolution 1H NMR spectroscopy. Analytica Chimica Acta 585 (1), 110–119.
Cao, R, Kobayashi, Y, Nonaka, A, Miyata, Y, Tanaka, K, Tanaka, T, Matsui, T., 2015. NMR spectroscopic and quantum mechanical analyses of enhanced solubilization of hesperidin by theasinensin A. Pharmaceutical research 32 (7), 2301–2309.
Chaudhry, V, Hussain, Z, Pandey, A, Khan, R, Srivastava, A., 2016. Isolation and characterization of hesperidin from the dried orange peel. International Journal of Research in Pharmacy and Science 6 (2), 15–18.
Chen, J, Luo, X, Qiu, H, Mackey, V, Sun, L, Ouyang, X., 2018. Drug discovery and drug marketing with the critical roles of modern administration. American journal of translational research 10 (12), 4302.
Cushnie, TT, Lamb, AJ., 2005. Antimicrobial activity of flavonoids. International journal of antimicrobial agents 26 (5), 343–356.
Daina, A, Michielin, O, Zoete, V., 2017. SwissADME: a free web tool to evaluate pharmacokinetics, drug-likeness and medicinal chemistry friendliness of small molecules. Scientific reports 7 (1), 1–13.
Dang, BN, Graham, DY., 2017. Helicobacter pylori infection and antibiotic resistance: a WHO high priority? Nature Reviews Gastroenterology & Hepatology 14 (7), 383–384.
Dariya B Nagaraju GP. Understanding novel COVID-19: its impact on organ failure and risk assessment for diabetic and cancer patients. Cytokine & growth factor reviews 2020.

de Mendonça, MA, Ribeiro, AR, AKd, Lima, Bezerra, GB, Pinheiro, MS, de Albuquerque-Júnior, RL, Gomes, MZ, Padilha, FF, Thomazzi, SM, Novellino, E., 2020. Red propolis and its dyslipidemic regulator formononetin: evaluation of antioxidant activity and gastroprotective effects in rat model of gastric ulcer. Nutrients 12 (10), 2951.
Debraekeleer, A, Remaut, H., 2018. Future perspective for potential Helicobacter pylori eradication therapies. Future microbiology 13 (06), 671–687.
Filocamo, A, Bisignano, C, Ferlazzo, N, Cirmi, S, Mandalari, G, Navarra, M., 2015. In vitro effect of bergamot (Citrus bergamia) juice against cag A-positive and-negative clinical isolates of Helicobacter pylori. BMC complementary and alternative medicine 15 (1), 256.
Fong, YH, Wong, HC, Yuen, MH, Lau, PH, Chen, YW, Wong, KB., 2013. Structure of UreG/UreF/UreH complex reveals how urease accessory proteins facilitate maturation of Helicobacter pylori urease. PLoS biology 11 (10), e1001678.
Gao, H, Chen, Y, Ma, H, Zeng, J, Li, G., 2014. Preparation and characterization of hesperidin-PEG 6000 complex. J Chem Soc Pakistan 36, 848–851.
Gardana, C, Nalin, F, Simonetti, P., 2008. Evaluation of flavonoids and furanocoumarins from Citrus bergamia (bergamot) juice and identification of new compounds. Molecules 13 (9), 2220–2228.
González, A, Salillas, S, Velázquez-Campoy, A, Angarica, VE, Fillat, MF, Sancho, J, Lanas, Á., 2019. Identifying potential novel drugs against Helicobacter pylori by targeting the essential response regulator HsrA. Scientific reports 9 (1), 1–13.
Górniak, I, Bartoszewski, R, Króliczewski, J., 2019. Comprehensive review of antimicrobial activities of plant flavonoids. Phytochemistry Reviews 18 (1), 241–272.
Hajialyani, M, Hosein Farzaei, M, Echeverría, J, Nabavi, SM, Uriarte, E, Sobarzo-Sánchez, E, 2019. Hesperidin as a neuroprotective agent: a review of animal and clinical evidence. Molecules 24 (3), 648.
Hooi JK, Lai WY, Ng WK, Suen MM, Underwood FE, Tanyingoh D, Malfertheiner P, Graham DY, WS V, Wong JC. Grant Support: Nil. 2017.
Husak, L, Dakhym, I, Marchyshyn, S, Demydyak, O, Kyryliv, M, 2017. Determination of phenolic compounds from Stachys sieboldii MIQ. herb and tubers. The Pharm Innov J 6 (9), 450–453.
Imran, M, Waqar, S, Ogata, K, Ahmed, M, Noreen, Z, Javed, S, Bibi, N, Bokhari, H, Amjad, A, Muddassar, M., 2020. Identification of novel bacterial urease inhibitors through molecular shape and structure based virtual screening approaches. RSC Advances 10 (27), 16061–16070.
Kang, S, Pinault, M, Pfefferle, LD, Elimelech, M., 2007. Single-walled carbon nanotubes exhibit strong antimicrobial activity. Langmuir 23 (17), 8670–8673.
Kataria, R, Khatkar, A., 2019. Molecular docking, synthesis, kinetics study, structure–activity relationship and ADMET analysis of morin analogous as Helicobacter pylori urease inhibitors. BMC chemistry 13 (1), 45.
Katarzyna, M., 2013. Inhibitors of bacterial and plants urease. Acta Universitatis Lodziensis Folia Biologica et Oecologica (09).
Khan S, Sharaf M, Ahmed I, Khan TU, Shabana S, Arif M, Kazmi SSUH, Liu C. Potential utility of nano-based treatment approaches to address the risk of Helicobacter pylori. Expert Review of Anti-infective Therapy 2021:1-18.
Kim, HW, Woo, HJ, Yang, JY, Kim, J-B, Kim, S-H., 2021. Hesperetin Inhibits Expression of Virulence Factors and Growth of Helicobacter pylori. International Journal of Molecular Sciences 22 (18), 10035.
Kim, S, Chen, J, Cheng, T, Gindulyte, A, He, J, He, S, Li, Q, Shoemaker, BA, Thiessen, PA, Yu, B, Zaslavsky, L, Zhang, J, Bolton, EE., 2019. PubChem 2019 update: improved access to chemical data. Nucleic acids research 47 (D1), D1102–D1109.
Krajewska, B, Brindell, M., 2016. Thermodynamic study of competitive inhibitors' binding to urease. Journal of Thermal Analysis and Calorimetry 123 (3), 2427–2439.
Laskowski, RA., 2009. PDBsum new things. Nucleic Acids Res 37, D355–D359. Database issue.
Lee, Y-S, Huh, J-Y, Nam, S-H, Moon, S-K, Lee, S-B, 2012. Enzymatic bioconversion of citrus hesperidin by Aspergillus sojae naringinase: Enhanced solubility of hesperetin-7-O-glucoside with in vitro inhibition of human intestinal maltase, HMG-CoA reductase, and growth of Helicobacter pylori. Food chemistry 135 (4), 2253–2259.
Li, S, Wang, Z, Wei, Y, Wu, C, Gao, S, Jiang, H, Zhao, X, Yan, H, Wang, X., 2013. Antimicrobial activity of a ferrocene-substituted carborane derivative targeting multidrug-resistant infection. Biomaterials 34 (4), 902–911.
Malfertheiner, P, Megraud, F, O'morain, C, Gisbert, J, Kuipers, E, Axon, A, Bazzoli, F, Gasbarrini, A, Atherton, J, Graham, DY., 2017. Management of Helicobacter pylori infection—the Maastricht V/Florence consensus report. Gut 66 (1), 6–30.
Maltese, F, Erkelens, C, van der Kooy, F, Choi, YH, Verpoorte, R., 2009. Identification of natural epimeric flavanone glycosides by NMR spectroscopy. Food Chemistry 116 (2), 575–579.
Marchyshyn, S, Hudz, N, Dakhym, I, Husak, L, Mishchenko, L., 2017. Analysis of phenolic compounds from Polymnia sonchifolia Poepp. & Endl. leaves by HPLC-method. The Pharma Innovation 6 (7), 980. Part G.
Mark PNilsson, L., 2001. Structure and dynamics of the TIP3P, SPC, and SPC/E water models at 298 K. The Journal of Physical Chemistry A 105 (43), 9954–9960.
Matysiak-Budnik TMégraud, F., 2006. Helicobacter pylori infection and gastric cancer. European journal of cancer 42 (6), 708–716.
Mishra, A, Jain, A, Arora, N., 2016. Mapping B-cell epitopes of major and minor peanut allergens and identifying residues contributing to IgE binding. Journal of the Science of Food and Agriculture 96 (2), 539–547.
Moon, SH, Lee, JH, Kim, KT, Park, YS, Nah, SY, Ahn, DU, Paik, HD., 2013. Antimicrobial effect of 7-O-butylnaringenin, a novel flavonoid, and various natural flavonoids against Helicobacter pylori strains. International journal of environmental research and public health 10 (11), 5459–5469.
Naif, M, AIsmail, RH., 2018. Detection of Some Types of Bacteria in Patients with Kidney Stones and the Use of Corn Silk Extracts to Effectively Inhibit the Urease Enzyme in Klebsiella Species. Int J Curr Microbiol App Sci 7 (8), 545–554.
Parreira, P, Fátima Duarte, M, Reis, CA, Martins, MCL, 2016. Helicobacter pylori infection: A brief overview on alternative natural treatments to conventional therapy. Critical reviews in microbiology 42 (1), 94–105.
Parreira P, Seabra CL, Lopes-de-Campos D, Martins MCL. Nonantibiotic-Based Therapeutics Targeting Helicobacter pylori: From Nature to the Lab. Helicobacter Pylori-New Approaches of an Old Human Microorganism: IntechOpen; 2018.
Piazuelo, MB, Epplein, M, Correa, P., 2010. Gastric cancer: an infectious disease. Infectious Disease Clinics 24 (4), 853–869.
Salehi, B, Sharopov, F, Martorell, M, Rajkovic, J, Ademiluyi, AO, Sharifi-Rad, M, Fokou, PVT, Martins, N, Iriti, M, Sharifi-Rad, J., 2018. Phytochemicals in Helicobacter pylori infections: What are we doing now? International journal of molecular sciences 19 (8), 2361.
Savoldi, A, Carrara, E, Graham, DY, Conti, M, Tacconelli, E., 2018. Prevalence of antibiotic resistance in Helicobacter pylori: a systematic review and meta-analysis in World Health Organization regions. Gastroenterology 155 (5), 1372–1382 e17.
Seabra, CL, Nunes, C, Gomez-Lazaro, M, Correia, M, Machado, JC, Gonçalves, IC, Reis, CA, Reis, S, Martins, MCL., 2017. Docosahexaenoic acid loaded lipid nanoparticles with bactericidal activity against Helicobacter pylori. International journal of pharmaceutics 519 (1-2), 128–137.
Selim, MS, Samak, NA, Hao, Z, Xing, J., 2020. Facile design of reduced graphene oxide decorated with Cu2O nanocube composite as antibiofilm active material. Materials Chemistry and Physics 239, 122300.
Sharaf, M, Arif, M, Khan, S, Abdalla, M, Shabana, S, Chi, Z, Liu, C., 2021a. Co-delivery of hesperidin and clarithromycin in a nanostructured lipid carrier for the eradication of Helicobacter pylori in vitro. Bioorganic Chemistry, 104896.
Sharaf, M, Hamouda, H, Shabana, S, Khan, S, Arif, M, Rozan, HE, Abdalla, M, Chi, Z, Liu, C., 2021b. Design of lipid-based nanocarrier for drug delivery has a double therapy for six common pathogens eradication. Colloids and Surfaces A: Physicochemical and Engineering Aspects, 126662.
Sheng, M, Valco, D, Tucker, C, Cayo, E, Lopez, T., 2019. Practical Use of Differential Scanning Calorimetry for Thermal Stability Hazard Evaluation. Organic Process Research & Development 23 (10), 2200–2209.
Shi, S, Huang, K, Zhang, Y, Liu, S., 2008. Preparative isolation and purification of two flavonoid glycosides from Taraxacum mongolicum by high-speed counter-current chromatography. Separation and purification technology 60 (1), 81–85.
Shin, S, Bajpai, V, Kim, H, Kang, S., 2007. Antibacterial activity of eicosapentaenoic acid (EPA) against foodborne and food spoilage microorganisms. LWT-Food Science and. Technology 40 (9), 1515–1519.
Tanaka, T, Kawase, M, Tani, S., 2003. Urease inhibitory activity of simple α, β-unsaturated ketones. Life sciences 73 (23), 2985–2990.
Trott OOlson, AJ., 2010. AutoDock Vina: improving the speed and accuracy of docking with a new scoring function, efficient optimization, and multithreading. Journal of computational chemistry 31 (2), 455–461.
Tshibangu-Kabamba, E, Yamaoka, Y., 2021. Helicobacter pylori infection and antibiotic resistance—from biology to clinical implications. Nature Reviews Gastroenterology & Hepatology 1–17.
Wu, D, Kong, Y, Han, C, Chen, J, Hu, L, Jiang, H, Shen, X., 2008. D-Alanine: D-alanine ligase as a new target for the flavonoids quercetin and apigenin. International journal of antimicrobial agents 32 (5), 421–426.
Yan, J, Peng, C, Chen, P, Zhang, W, Jiang, C, Sang, S, Zhu, W, Yuan, Y, Hong, Y, Yao, M., 2022. In-vitro anti-Helicobacter pylori activity and preliminary mechanism of action of Canarium album Raeusch. fruit extracts. Journal of Ethnopharmacology 283, 114578.
Yu, X-D, Zheng, R-B, Xie, J-H, Su, J-Y, Huang, X-Q, Wang, Y-H, Zheng, Y-F, Mo, Z-Z, Wu, X-L, Wu, D-W., 2015. Biological evaluation and molecular docking of baicalin and scutellarin as Helicobacter pylori urease inhibitors. Journal of ethnopharmacology 162, 69–78.
Zgurskaya, HI, Weeks, JW, Ntreh, AT, Nickels, LM, Wolloscheck, D., 2015. Mechanism of coupling drug transport reactions located in two different membranes. Frontiers in microbiology 6, 100.
Zhang, L, Kong, Y, Wu, D, Zhang, H, Wu, J, Chen, J, Ding, J, Hu, L, Jiang, H, Shen, X., 2008. Three flavonoids targeting the β-hydroxyacyl-acyl carrier protein dehydratase from Helicobacter pylori: crystal structure characterization with enzymatic inhibition assay. Protein Science 17 (11), 1971–1978.